On the key role of crack surface area on the lifetime of arbitrarily shaped flat cracks

L. David, V. Lazarus

Version of Record: https://www.sciencedirect.com/science/article/pii/S0142112321003686
Manuscript_4400c089b80453ed0e58d039a55a01fc

On the key role of crack surface area on the lifetime of arbitrary shaped flat cracks

L. David[a,b], V. Lazarus[a]

[a] *IMSIA, ENSTA Paris, CNRS, EDF, CEA, Institut Polytechnique de Paris, 828 boulevard des Maréchaux, 91762 Palaiseau cedex, France*
[b] *Safran Aircraft Engines, Site de Villaroche, Rond-point René Ravaud - Réau, 77550 Moissy-Cramayel, France*

Abstract

Accurate fatigue lifetime prediction is a central element in many industries. Often, a damage tolerant approach is used to ensure that some given imperfections are safe. In this context, these lifetime predictions are frequently made using simplified crack geometries leading to costly conservatism. In particular for a closed crack front, a circular or elliptical crack enclosing the real defect is generally used leading to an underestimation of the real lifetime. Using an iterative perturbation method to simulate the fatigue growth of many tensile complexly shaped cracks, we show that in the absence of any additional complexity, (i) the front quickly becomes circular; (ii) its evolution with the number of loading cycles can be obtained analytically using a circular crack of same area as the original distorted defect. In practice, it means that replacing a complex crack front shape with this simple, analytically solvable configuration is an effective way to improve predictions and that it is not useful to invoke more complex shapes such as elliptical cracks. These take-home messages are illustrated by an example from the aviation industry.

Preprint submitted to International Journal of Fatigue *23rd July 2021*

Keywords: Fatigue, Lifetime assessment, Mode I crack, Perturbative method, Damage tolerance

---

Contents

Introduction

Accurate lifetime prediction is crucial in many domains: hydroelectric dams, nuclear power plants, bridges, aircraft, railways to cite a few. Overestimating the lifetime in comparison to the real one can lead to catastrophic consequences, whereas underestimation leads to additional environmental costs. Refined models may help to increase the reliability of the forecasting while limiting the effects on the ecological footprint. In particular in a damage tolerance approach, where the presence of cracks or defects are assumed, whether due to manufacturing or detected at a later stage of use, accurate crack growth calculations are necessary to ensure appropriate safety: it determines the time span to next inspection and the moment where reparation becomes mandatory. Yet these predictions are generally done using simplified, mostly 2D, geometries: straight, circular cracks or elliptical cracks as those indexed in handbooks [1, 2]. But, as shown both in postmortem fractography and initial defect observation, the real shape of the crack is mostly much more complex.

The aim here is to focus on the influence of the crack front shape on lifetime predictions. Hence, we consider a planar crack embedded in an infinite, linear elastic isotropic material, loaded by a uniform cyclic tensile stress. We assume the crack advances following a simple Paris' law. In this way, the sole complexity comes from a possible distorted crack front, avoiding any additional effect that may be induced by the finite size of the domain, multimode loading, non flatness of the crack, material anisotropy or nonlinearity, complex loading condition and history, or sophisticated propagation laws.

Methods based on Finite Elements are not suitable for this purpose since a finite size body has to be considered. Therefore, boundary effects can not be excluded unless working with a small crack in a huge body, but then the effects of the front distortions are impossible to catch accurately. An alternative and efficient way to deal with it is to resort to perturbation approaches (see [3] for a review). Assuming a flat crack and an infinite body, the method reduces the geometry involved in the problem to that of the crack front, so that the meshing operation is restricted to this line. Initiated by Bueckner [4] and Rice [5] at about the same time, it gives the variation of the Stress Intensity Factor (SIF) due to a small perturbation of the crack front. Applied iteratively, following a seminal idea of Rice [6], the SIF along an arbitrary large perturbed front can be computed.

The method has been implemented numerically by Bower and Ortiz as described in [7], and used in the case of propagation through an array of tough microparticles [8], tough particles and microcracks [9], as well as non-uniform remote stresses and residual stresses [10]. Lazarus and co-workers have adapted the method to study the propagation of closed crack fronts (circular, elliptical, rectangular, heart-shaped) in a homogeneous material in both mode I [11] and mode II+III [12] loading conditions, but also for a tensile crack propagating in a highly heterogeneous solid [13] and for the coalescence of two circular cracks [14].

A first rough study of the influence of the shape on the evolution of the crack size with the number of loading cycles N has been done in [11] to illustrate the possibility of the perturbation approach to deal with this issue. Here, thanks to the systematization of the study to an extensive panel of

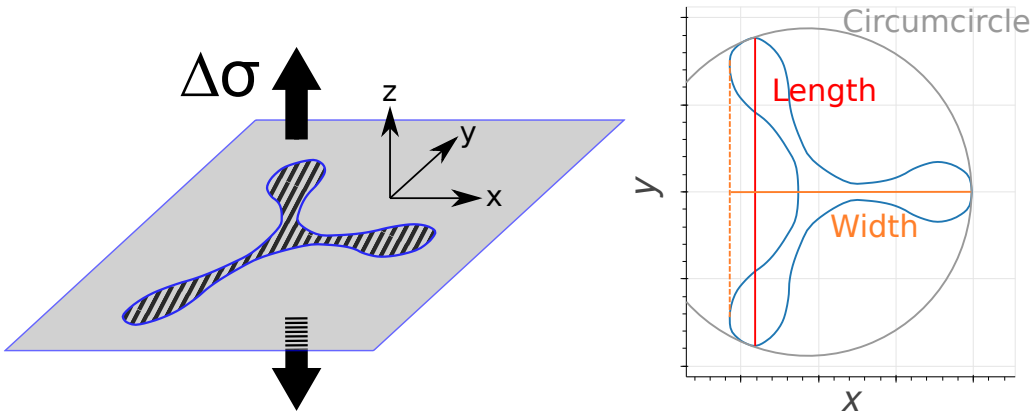

(a) Plane crack loaded in mode I only (tensile stress perpendicular to the crack plane)

(b) Definition of the length and width of a crack.

Figure 1: Problem statement and definition of some characteristic lengths.

crack front shapes, the influence of the choice of the crack size definition (perimeter, surface, width, length, circumcircle diameter) on the results is discussed systematically. We show first that perimeter and width are not admissible options since they may decrease during propagation, and second that under the assumptions set out below, the lifetime predictions are weakly dependent on the precise crack shape provided that the crack surface area is chosen as the representative size of a crack. In practice, it means that the lifetime can be computed analytically using a circular crack of same area and that it is not worth to invoke more complex crack shapes as ellipses for instance. We use the case of shrinkage cavities to illustrate the results for practical engineering purposes.

1. Methods

1.1. Problem statement

Consider a flat crack in an infinite linear elastic isotropic body subjected remotely to a uniform tensile cyclic stress of constant amplitude $\Delta\sigma$ (Fig. 1a). Suppose that the normal crack advance at each point s is ruled by Paris' law:

$$\frac{\mathrm{d}a(s)}{\mathrm{d}N} = C\left(\Delta K(s)\right)^n, \tag{1}$$

$\Delta K(s)$ being the amplitude of the SIF during one cycle.

If the crack front is a circle of radius r, the SIF K_0 is uniform along the crack front:

$$\Delta K_0 = 2\Delta\sigma\sqrt{r/\pi}, \tag{2}$$

resulting in a uniform crack advance, so that the shape remains the same during propagation. If the crack front is tortuous, $K(s)$ is not uniform, the shape of the front evolves during propagation involving a succession of complex crack forms for which the values of $K(s)$ have to be updated.

Herein, we aim to replace this complex 3D evolution problem that has to be solved for each point of the crack front, with the one of the radius evolution of a circular crack, that is to replace Eq. (1) with a unique equation:

$$\frac{\mathrm{d}r}{\mathrm{d}N} = C(\Delta K_0)^n \tag{3}$$

Several choices to define the equivalent radius r are possible, they will be introduced in next section.

1.2. How to define the equivalent crack size r?

Let us discuss several options for the choice of r to be used in Eq. 3. Monitoring the position of a particular point, as was done in the prelimin-

ary studies of [11], is a subjective way to define this variable. It can't be generalized to arbitrary shapes. We propose five objective measurements to define the size : area, perimeter, length, width, and the diameter of the circumscribed circle. While the precise definition of the area, perimeter, and circumscribed circle is straightforward, it is less trivial for the length and width. Herein, the *length* of a crack is defined to be the greatest length between any two points of the crack front. The *width* is taken to be the distance between the two points the furthest away along an axis perpendicular to the length (Fig. 1b). Each of these measurements will be used to define variables representing the crack size.

In order to have sizes which equalize to the radius if the crack is circular, we define length (L), width (W), perimeter (P), circumcircle diameter (C), or surface area(S) based sizes respectively by :

$$r \equiv \frac{L}{2} \qquad r \equiv \frac{W}{2} \qquad r \equiv \frac{P}{2\pi} \qquad r \equiv \frac{C}{2} \qquad r \equiv \sqrt{\frac{S}{\pi}} \tag{4}$$

Among them, the surface-based size has a special significance later on, this is why we introduce the following specific notation:

$$a \equiv \sqrt{\frac{S}{\pi}} \tag{5}$$

These equivalent sizes will be used to post-process the results of the simulations of crack propagation made using the method shown in the next section.

1.3. The iterative perturbation approach

In short, the perturbative method is based on the weight-function theory developed by Rice [6], and permits the computation of the variation of the

Stress Intensity Factor (SIF) along a given plane crack caused by some small perturbation of the crack front, knowing the SIF along the original front. This method makes no assumptions on the crack shape other than its flatness, which makes it suitable to study arbitrarily shaped cracks.

Denote $\mathcal{F}$ the crack front, s the curvilinear abscissa[1] along $\mathcal{F}$, $W(s, s')$, an influence function derived from the SIF at point s when a doublet of point forces is applied in the vicinity of s'. By using the linearity of the elasticity problem, we introduce a dimensionless SIF $\kappa(s)$, that depends only on the crack shape and is independent of the initial crack size and of the loading amplitude:

$$\kappa(s) = \frac{K(s)}{\Delta\sigma\sqrt{r_0}} \tag{6}$$

For any small normal perturbation $\delta a(s)$ of the crack front, the variation of $\delta\kappa(s_0)$ that will arise for any point at abscissa s_0, is given to the first order in δa by:

$$\delta\kappa(s_0) = \frac{1}{2\pi}\mathrm{PV}\int_{\mathcal{F}} \frac{W(s_0, s)}{D^2(s_0, s)}\kappa(s)(\delta a(s) - \delta_* a(s))\mathrm{d}s, \tag{7}$$

where $D(s, s')$ is the euclidean distance between points s and s', and $\delta_* a(s)$ is a normal advance that preserves the shape and size of the front and verifies $\delta a(s_0) = \delta_* a(s_0)$. This condition ensures that the Principal Value integral $\mathrm{PV}\int$ exists.

Similarly, an analogous formula for W is:

$$\delta W(s_0, s_1) = \frac{D^2(s_0, s_1)}{2\pi} PV \int_{\mathcal{F}} \frac{W(s_0, s)W(s_1, s)}{D^2(s_0, s)D^2(s_1, s)}(\delta a(s) - \delta_{**} a(s))\mathrm{d}s, \tag{8}$$

[1]Such that $\left\|\frac{\mathrm{d}\mathbf{x}}{\mathrm{d}s}\right\| = 1$, where $\mathbf{x}(s)$ is the point of the front at the abscissa s

with $\delta_{**}a(s)$ any normal advance that preserves the shape of the front and verifies $\delta a(s_0) = \delta_{**}a(s_0)$ and $\delta a(s_1) = \delta_{**}a(s_1)$.

From this, with multiple successive perturbations, any propagation of a crack front can be simulated if we know the initial κ and W. Moreover, we can compute κ and W for any closed crack front by perturbing a circle for which it is known [15] that $W(s, s') = 1$, and $\kappa(s) = 2\sqrt{\frac{r}{\pi r_0}}$, r being the radius. Therefore, the iterative perturbation method can be used to simulate the propagation and predict the evolution of a crack regardless of its shape in two stages, as illustrated in Fig. 2 for the case of a rectangular crack:

1. Initialization (Fig. 2a): starting from a circle and perturbing it in order to get K and W along the desired shape.
2. Propagation (Fig. 2b): applying successive perturbations that correspond to the advance of the crack given by a Paris' law (Eq. 1) as done here, or more generally any fatigue propagation law based on the SIF.

In this process, the sole mesh required is that of the crack front $\mathcal{F}$. For more details, the readers may refer to [11], which lays the foundations of the simulation software used here. Several improvements have nevertheless been implemented, and will be the subject of another article focusing on the numerical methods developed.

1.4. Tested crack shapes

To ensure that we appraise each choice of equivalent crack fairly, it is important to test a large variety of crack shapes. To verify this requirement, we use five types of crack shapes in our study : a collection of ellipses and rectangles with aspect ratios varying from 0.2 to 1, two kinds of heart-shaped

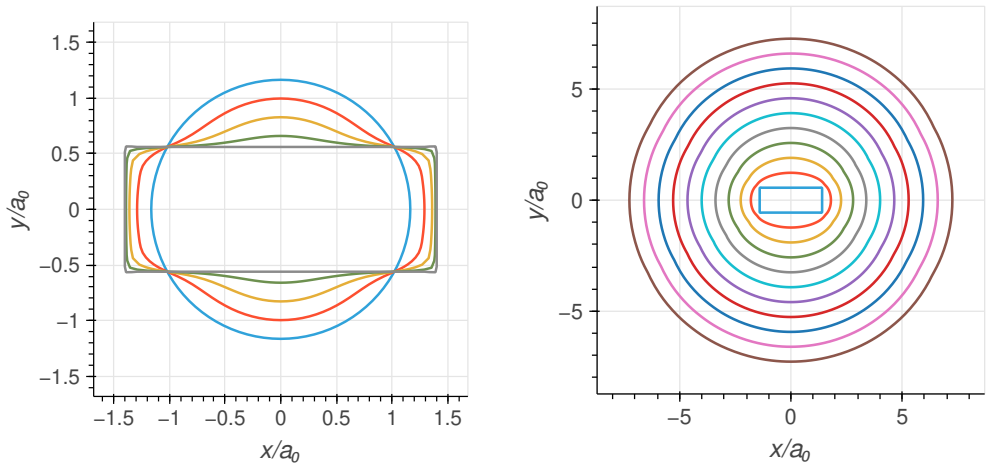

(a) Initialization stage

(b) Propagation stage ($n = 3$)

Figure 2: Selection of some crack fronts encountered during the initialization and propagation stages of the numerical method in the case of a rectangular crack.

cracks with cusp angles varying from 0° to 180°, flower-shaped cracks with 2 to 8 petals, and finally the external shape of letters and numbers. Figure 3 gives a patchwork of these shapes. A total of 109 crack shapes are considered. We use five values of n ($n = 1, 2, 3, 4, 5$) to cover the range of most materials [16]. This makes a total of 545 crack propagation simulations.

1.5. Numerical implementation

Since the body is assumed to be infinite, the lengths can be rescaled by the initial size r_0 of the crack. The loading amplitude $\Delta\sigma$ being constant over the cycles, Eq. 1 can be rewritten using the definition of $\kappa(s)$ (Eq. 6):

$$\frac{\mathrm{d}a(s)/r_0}{\mathrm{d}\overline{N}} = \kappa(s)^n, \tag{9}$$

where

$$\overline{N} = NC(\Delta\sigma)^n r_0^{n/2-1} \tag{10}$$

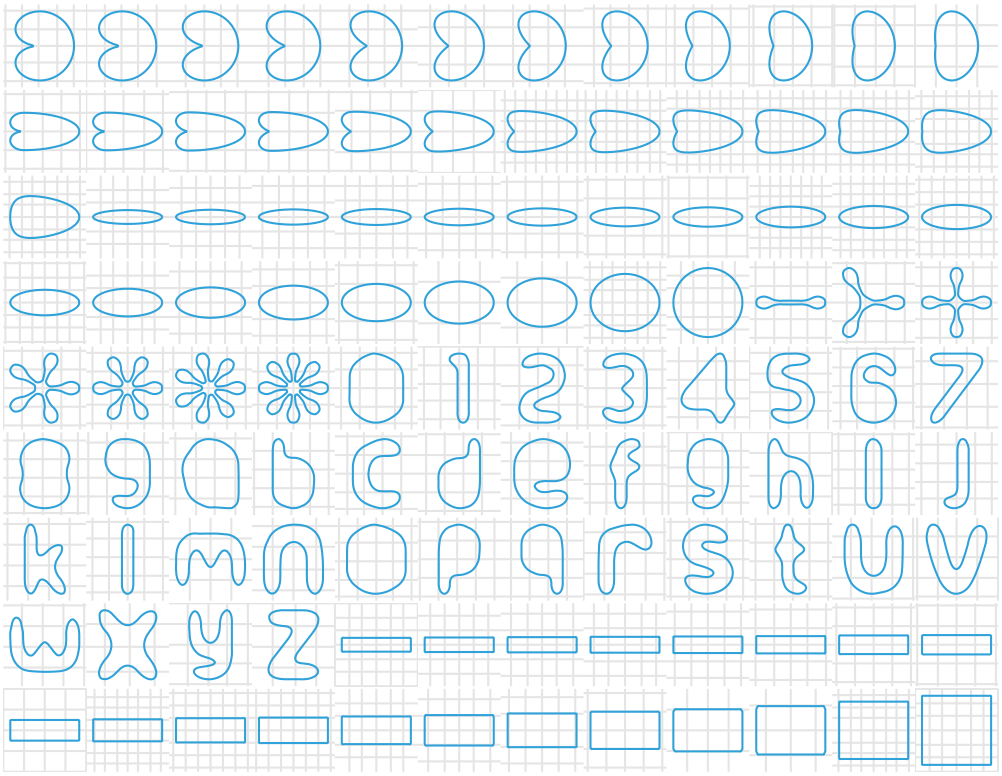

Figure 3: Patchwork of the simulated shapes

The number of parameters involved can thus be reduced to the sole parameter n.

In practice, for a given initial crack shape and value of n, Eq. 9 is solved iteratively to get the evolution of the crack shape versus $\overline{N}$. In this process, $\kappa(s)$ is updated using the perturbation approach presented in Section 1.3 and the evolution of the crack front is obtained from the advance law (Eq. 1) applied at each point of the front. The evolution of r/r_0 with $\overline{N}$ is extracted from these successive crack positions for each of the definition of r introduced in Eqs. 4: the length taking the maximum of $D(s, s_0)$; the width can then be obtained in a straightforward way (see Fig. 1b); the perimeter and area

by integration along the front of the curvilinear abscissa ($P = \int_{\mathcal{F}} \mathrm{d}s$; $S = \int_{\mathcal{F}} \frac{1}{2} \left\| \mathbf{x}(s) \times \frac{\mathrm{d}\mathbf{x}}{\mathrm{d}s} \right\| \mathrm{d}s$); the circumcircle radius using the method presented in [17].

1.6. Error estimation and inaccuracy of certain simulations

It happens that the perturbation method yields imprecise results, notably if the shape has many sections of high curvature. To exclude the simulations that are subject to large numerical errors, we need a way to assess the precision. In our problem, the values of $K_{\mathrm{num}}(s)$ at the final stage results from iterations on many cycles and may thus be error-stained. Yet, the final shape is always nearly circular (see Fig. 2 and several examples below), and it is possible to recalculate the SIF with a good accuracy (see Appendix A for a discussion of this accuracy) starting from the nearest circle since few iterations are then necessary. The value $K(s)$ obtained in this way, serves as reference to obtain an estimation of the relative numerical error E of the SIF defined by:

$$E = \frac{1}{s_{max}} \sqrt{\int_0^{s_{max}} \frac{\left(K_{\mathrm{num}}(s) - K(s)\right)^2}{K_{\mathrm{m}}^2} \mathrm{d}s} \tag{11}$$

where K_{m} is taken to be the mean of $K(s)$ over the front.

We can then exclude all propagation that have an error above a certain threshold E_{th}. In this study, we choose arbitrarily $E_{th} = 0.05$. In practice, it led us to keep 462 of the initial 545 simulations.

2. Results

2.1. Evolution of a circular crack

For the reference case of a circular crack of radius r, $\kappa = 2\sqrt{\frac{r}{r_0\pi}}$ so that Eq. 9 becomes:

$$\frac{\mathrm{d}r/r_0}{\mathrm{d}\overline{N}} = \left(\frac{r}{r_0}\right)^{n/2} \left(\frac{2}{\sqrt{\pi}}\right)^{n} \tag{12}$$

For $n = 2$, the solution of this differential equation is:

$$\frac{r}{r_0} = \exp\left(\frac{4}{\pi}\overline{N}\right) \tag{13}$$

and for all other n:

$$\frac{r}{r_0} = \left(1 - 2^{n-1}\frac{n-2}{\pi^{n/2}}\overline{N}\right)^{\frac{-2}{n-2}} \tag{14}$$

2.2. All the shapes become circular after a transition phase

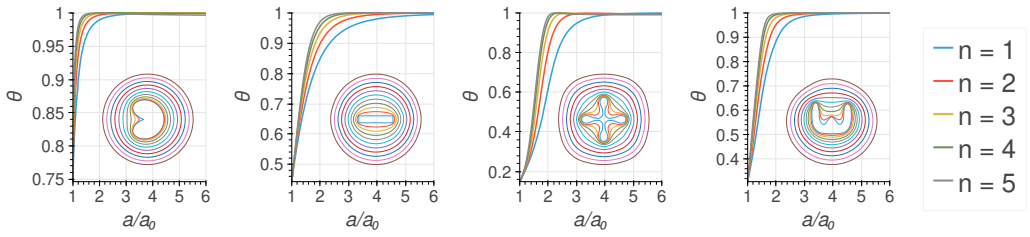

Figure 4: Evolution of the crack front shapes for a representative panel in the case $n = 3$. Evolution of the circularity as defined in Eq.15 for the same initial shape and different values of n. Whatever the shape and n, the shape quickly evolves toward a circle, and this evolution is faster when n is higher (from bottom to top, the curves are always ordered by growing n values).

Figure 4 gives a representative panel of the evolution of several crack shapes to illustrate that in all cases of Fig. 3 and for any value of $n = 1, 5$,

the crack deforms during propagation during a transitory phase until reaching a stationary self-sustained circular shape.

To quantify this affirmation, we use the circularity θ of the crack shape defined by

$$\theta = \frac{4\pi S}{P^2} \tag{15}$$

If the shape is circular $\theta = 1$. If not, the value departs from 1 in the range $[0; 1[$. In Fig. 4, while the crack shape progress is only given for $n = 3$ for each of the selected shape, the corresponding evolution of θ with a/a_0 is plotted for different values of n. We observe that it always reaches $\theta \simeq 1$ quickly. We also notice that the circularity gets closer to 1 more promptly if n is higher: it is expected since for higher n values, the influence of the SIF values (dependent on the crack shape) on the crack advance is stronger. Table 1 quantifies the growth a/a_0 that is required to be sure to escape the transition phase. While for $n = 2$ a growth of a factor of 3 is necessary, for $n = 5$ a factor of 2 is sufficient.

Paris exponent	1	2	3	4	5
(a/a_0)	3.3	2.7	2.4	2.1	1.8

Table 1: Crack growth required so that all cracks of Fig. 3 reach a circular state (set here at $\theta > 0.95$).

Now for practical purpose, it may be useful for a given shape and n, to estimate the number of cycles that are required to go from the initial form to the circular one. This can be done in two steps: first on Fig. 4 look for the value of a/a_0 for which θ reaches a targeted precision, for instance 0.95;

second to use Eq. (14) or (13) to get the corresponding $\overline{N}$, hence N thanks to Eq. (10). In this process, r/r_0 can be replaced by the critical value of a/a_0 since as will be seen later with the choice $r = a$, the relation between $\overline{N}$ and r/r_0 hardly depends on the crack shape.

2.3. Exclusion of the perimeter and the width as relevant size choices

In certain special cases, some sizes that we defined in Eqs. (4) have been observed to decrease. Such sizes are disqualified as a properly defined crack size is necessarily monotonic : fracture is indeed an irreversible process. Fig. 5 shows the evolution of the sizes for two special crack shapes that illustrate this behaviour: a rectangular crack to discard the width, and a flower shape one to discard the perimeter.

For rectangle shaped cracks, at the beginning, the width is defined along a perpendicular line to a diagonal that defines the length (maximum distance). But after a while, it is defined as the small axis of the ellipse-like shape that appears after some propagation. This transition in the orientation that defines the width can be visualized in the inset of Fig. 5a. It explains the small decrease of r/r_0 with $\overline{N}$ observed in this figure (green line).

For flower-shaped cracks with enough petals, the crack advance is observed to be smaller at the tips of the petals than in the most remote zones of the front (Fig. 5d). This is because the SIF at the peaks is smaller than at the troughs [13]. This difference in crack advance explains the decrease of r/r_0 with $\overline{N}$ observed in Fig. 5b when r is defined using the perimeter (grey line).

The three remaining sizes are monotonic in all circumstances : it is obvious for the surface or circumcircle-based sizes. For the length-based, it is

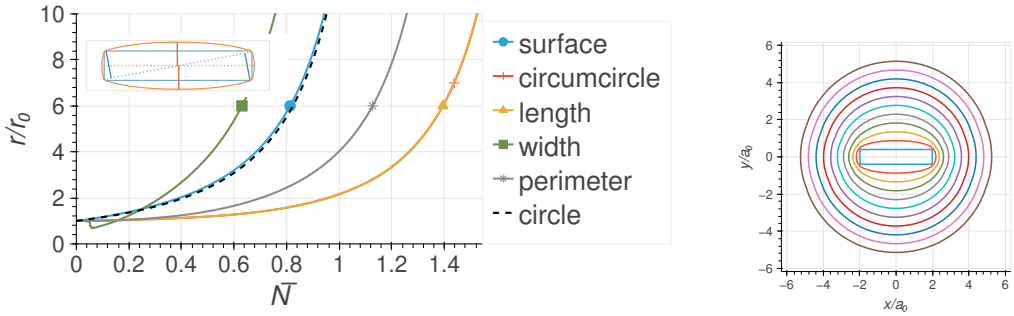

(a) Rectangular crack with ratio 5 : 1

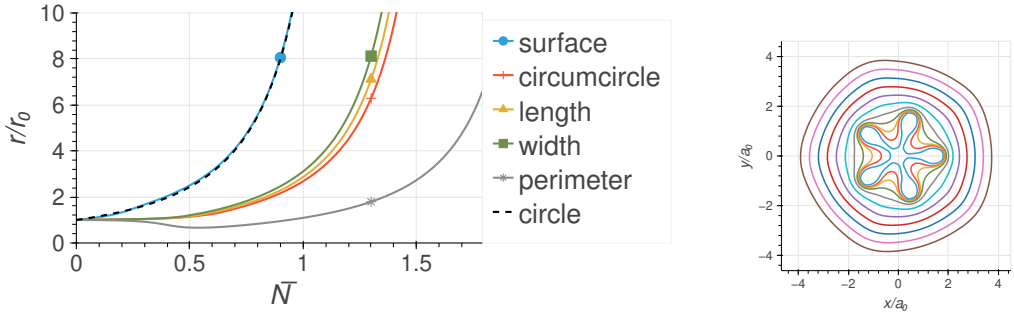

(b) 5-petals flower shape

Figure 5: Examples of shapes discarding perimeter and width based sizes since they yield decreasing evolutions ($n = 3$ here). Right: some successive positions of the front during propagation. Left: full lines represent the evolution of the sizes determined from the real crack evolution following the method described in Section 1.5, and the dotted line the evolution of a circle (Eq. 14). For the rectangle, the insert explains why the width is decreasing : as the shape transitions from a rectangle to an ellipse-like shape, the longest diagonal that defines the length (dotted line) rotates and so the width (solid straight lines) changes drastically.

linked to the facts that (i) the length of a crack is the same as the length of its convex hull and (ii) convex hull of a crack after propagation completely contains all the previous convex hulls. Hence, of the five sizes introduces in Eqs. (4), only three should be retained to preserve irreversibility: surface, circumcircle and length based ones.

2.4. Real crack versus circular crack evolutions

The plots r/r_0 versus $\overline{N}$ are not convenient for comparisons in terms of size growth r versus loading cycle N, and notably to discuss the conservatism of a particular choice as we aim to do in this section, since r_0 depends on the choice of the size definition (Eq. 10). This is why a_0 is used instead of r_0 as length scale in Fig. 6, where a_0 is the initial value of a as defined in Eq. 5.

This figure shows the evolution of the three remaining sizes for a selection of shapes. As in Fig. 5, (i) the solid lines represent the evolution of the sizes computed from the real crack evolution as explained in Section 1.5; (ii) the dotted lines correspond to the evolution of the three sizes if the shape is circular (Eq. 14 since $n = 3$ in the figure). The initial point of each plot, r_0/a_0, are choice dependent. This explains why the dotted lines don't merge here, although it was the case in Fig. 5 thanks to the rescaling by r_0.

Let us define the lifetime as the number of cycles to increase the crack from its nominal size r_0 to a critical value r_c. If the shape of the crack has become circular at this point, it is obviously equivalent to define the final failure by targeting Irwin's threshold. As can be observed on Fig. 6, for the circumcircle and the length, the dotted lines are always located to the left of the full lines of the same colours. It means that lifetime predicted using these sizes underestimates the real one, hence are conservative. This result might

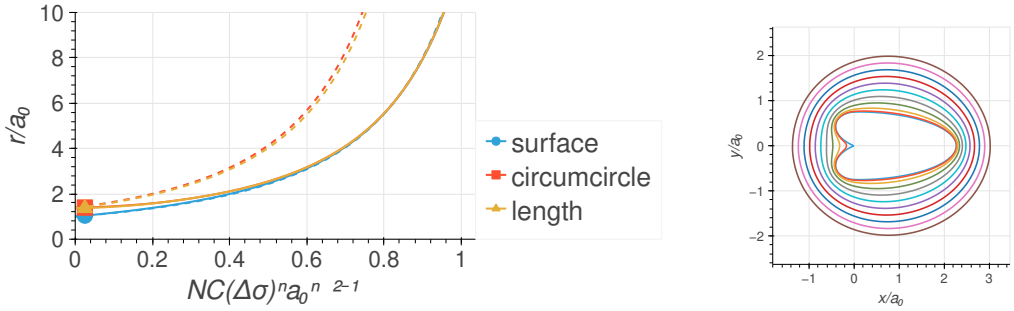

(a) Heart-shaped crack with a cusp angle of 45°.

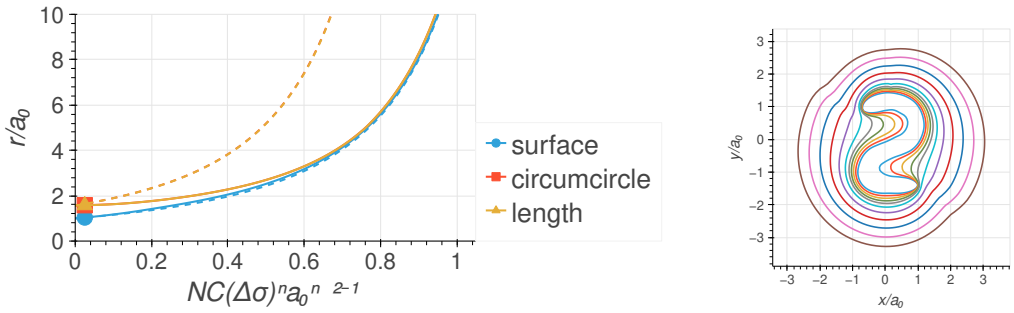

(b) 2-shaped crack.

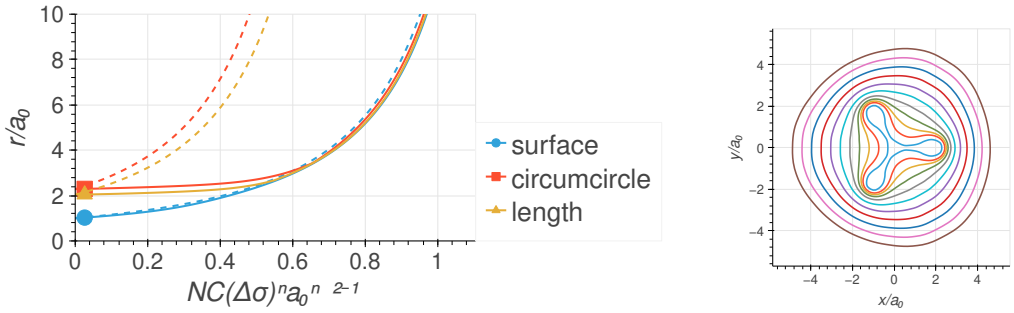

(c) Flower shaped crack with three petals.

Figure 6: Similar figures than in Fig. 5, but for other initial crack shapes and with rescaling by a_0 instead of r_0. The evolutions of the equivalent circles depend on the choice of the size definition since the initial values differ. Predictions taking the circumcircle and length based definitions are conservative. Surface based choice gives an evolution that is very close to the real one.

seem obvious as the substituted circular crack completely encloses the initial crack. However, it strongly relies on the fact that all the shapes studied here turn quickly into a circular one. One can not exclude a priori the existence of a crack shape that has the property of persisting sufficiently in a not circular one during propagation and that advance faster than the enclosing circular crack. We found no such shape in our study, while numerous fronts have been tested (Fig. 3).

The length-based size is often equal to the circumcircle-based one as illustrated by Fig. 6b. But in the cases where this equality does not hold (Fig. 6a,c), the length is inferior to the diameter of the circumcircle and the equivalent circular crack does not enclose the real crack. Therefore, lifetime predictions made with this reference size are still conservative, but less pessimistic than the ones made using the circumcircle.

The most remarkable observation, that will be deepened in next section, is that for the surface, dotted and full lines are very close, either slightly to the right or slightly to the left. It means that substituting a complexly shaped crack by a circular crack having the same area leads to lifetime predictions that are not always strictly conservative, but much closer to the reality than any other choice of size that we tested.

2.5. Equivalence between the real crack and a circular crack of same area

Figure 7 aims to compare the evolution of all the crack shapes with the one of a circular crack, for the different sizes defined in Eqs. (4). In this figure, the rescaling by r_0 is again relevant since the circular crack evolutions then merge on one single curve (dotted black lines) corresponding to Eq. (12). Each curve corresponds to the propagation of one crack from Fig. 3 and a

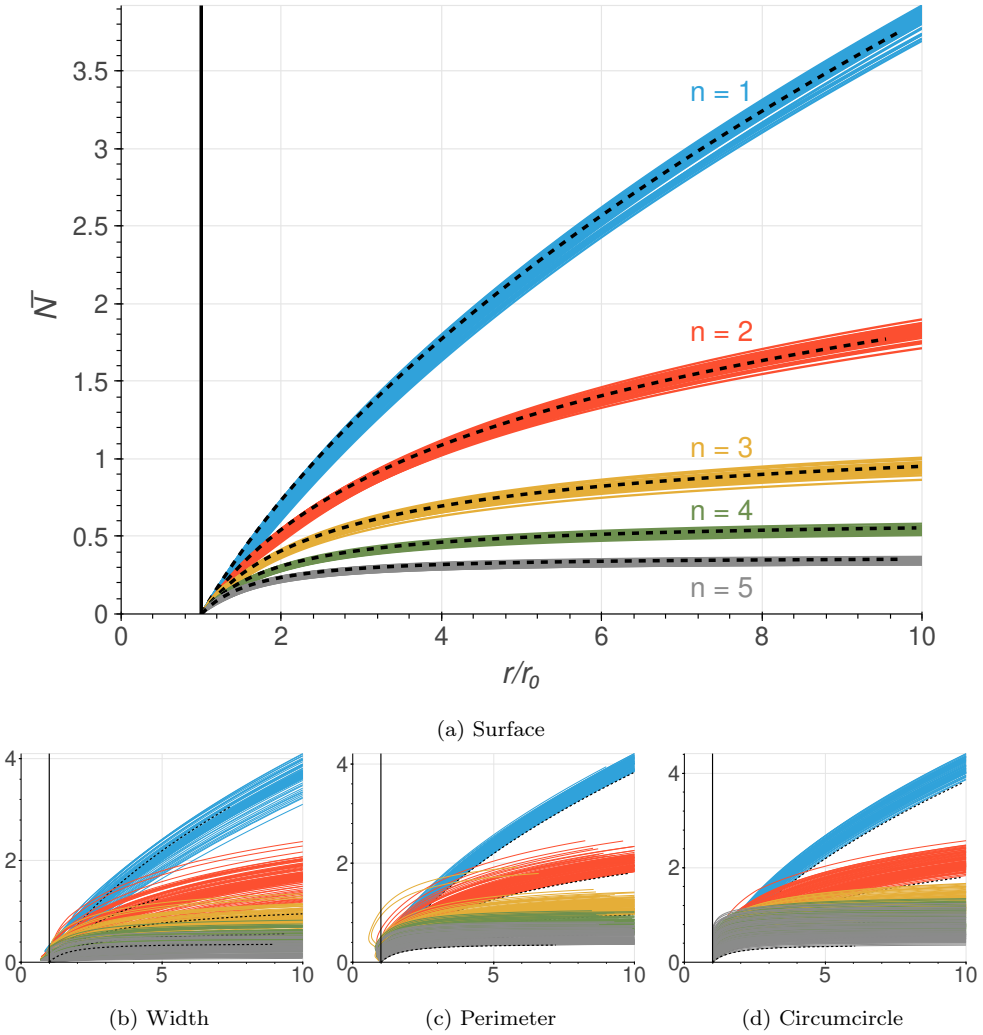

(a) Surface

(b) Width

(c) Perimeter

(d) Circumcircle

Figure 7: Impact of the choice of sizes on the crack evolution compared to a circle. The x and y labels and the colour code are the same for all figures and given only in (a) for readability. The figure showing the length-based size is not shown as it is almost identical to the circumcircle-based one. The vertical lines at $r/r_0 = 1$ show that many more shapes than the few examples shown in section 2.3 actually have decreasing width or perimeters.

given Paris' exponent n.

For the surface based choice $r = \sqrt{S/\pi}$ (Fig. 7a), we can clearly see five bundles of curves, corresponding to the five values of Paris' exponents n considered, which are grouped around the reference curve. In comparison, the evolution of the other sizes (width, perimeter, circumcircle) given in Figs. 7b, 7c, and 7d respectively are more dispersed and depend strongly on the crack shape. This shows that the evolution of the crack surface area has a weak dependency on the actual shape of the crack.

Even if not relevant as demonstrated in Section 2.3, we show width and perimeter based evolution anyway for two reasons. First, to underline their dispersion in comparison to the surface evolution. Second, to show once again that for width and perimeter (Figs. 7b, 7c), in contrary to the other cases (Figs. 7a, 7d), some unacceptable decrease of r/r_0 below 1 appear in many cases.

Evolutions shown in Fig. 7 supposes that the loading amplitude is constant. This assumption can be lifted to take into account complex load history by proceeding stepwise. Hence, the resulting evolution curves would still merge around the one obtained for a circular crack of same area.

The dispersion of the curves within the bundles of Fig. 7a has two possible origins : the effect of the crack shape and numerical inaccuracies. In Appendix B, we show that the dispersion within a bundle is to some extent caused by numerical inaccuracies so that the statement *whatever the front shape, the crack surface area evolves exactly like the one of a circular crack* may be right. However, since numerical errors can never be eliminated completely, one can not fully conclude: Only an analytical proof has the ability

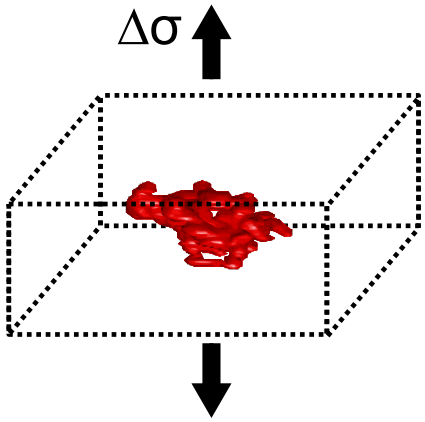

Figure 8: Tomographic image of a shrinkage cavity observed in a nickel alloy

to prove or disprove this affirmation.

2.6. Practical example : shrinkage cavities

To illustrate the usefulness of the method for practical engineering purposes, we use the example of shrinkage cavities, a type of defects that can arise in nickel alloys and are taken into account in damage tolerant design in aeronautics. The typical size of such defects is in the range of 0.1 to 1 mm.

A tomography image of such a defect is given in Fig. 8. We consider the 2D projection of these three-dimensional defect as the more noxious crack. For a numerical application, the following realistic case is considered: the initial area of the crack is 1 mm^2, the cyclic loading is between 0 and $\Delta\sigma =$ 500 MPa, Paris' law parameters are $n = 3$ and $C = 10^{-12}$ $\text{mm}^{-1/2}.\text{MPa}^{-3}$, the critical SIF is $K_c = 1500$ $\text{MPa}.\sqrt{\text{mm}}$.

We define the lifetime as the number of cycles from the initial situation until the Irwin threshold $K = K_c$ is reached at least at one crack front point. For a circular crack, this corresponds to $r_c = \pi \left(\frac{K_c}{2\Delta\sigma}\right)^2 \simeq 7.1$ mm.

In Fig. 9, the simulation using the perturbation approach is presented. As expected from Section 2.2, the front deforms until reaching a quasi-circular shape (Fig. 9a). We find numerically that Irwin's criterion is reached at one point after 10696 cycles. At this number of loading cycles, the sizes of the crack reach values very close to $r_c = 7.1$ mm (Fig. 9b), consistent with the fact that the crack is nearly circular at this stage.

We can easily analytically compute the lifetime of a circular crack having the same initial size as the real crack using Eqs. (10) and (14), with $r = r_c$ and r_0 obtained from the initial shape using different definition of r given in Eqs. 4. In this example, we only consider the surface-based size, and the circumcircle-based size, which is in this case equal to the length-based size. If we choose the surface-based size, the initial size of the crack is $r_0 = 0.56$ mm, that yields $\overline{N} = 1.00$ that is $N = 1.07 \times 10^4$ cycles (see blue dotted line in Fig. 9b). If instead we use the substitution of the real crack by the circular crack of same size using the circumcircle-based size, we would do the same calculations with $r_0 = 0.92$ mm which leads to a predicted lifetime of $N = 7420$ loading cycles (see red dotted line in Fig. 9b). It is conservative, as expected from Section 2.4.

As expected from Section 2.5, we obtain that the lifetime predicted analytically using the surface-based size is extremely close to the one found using the perturbation method with the real crack shape (a difference of only 6 cycles, that is 0.06% of the total lifetime) but without any computational cost, whereas the circumcircle-based size yields a prediction that is more than 30% less than the lifetime predicted using the actual crack shape. This means that there is plenty of room to refine lifetime assessments and

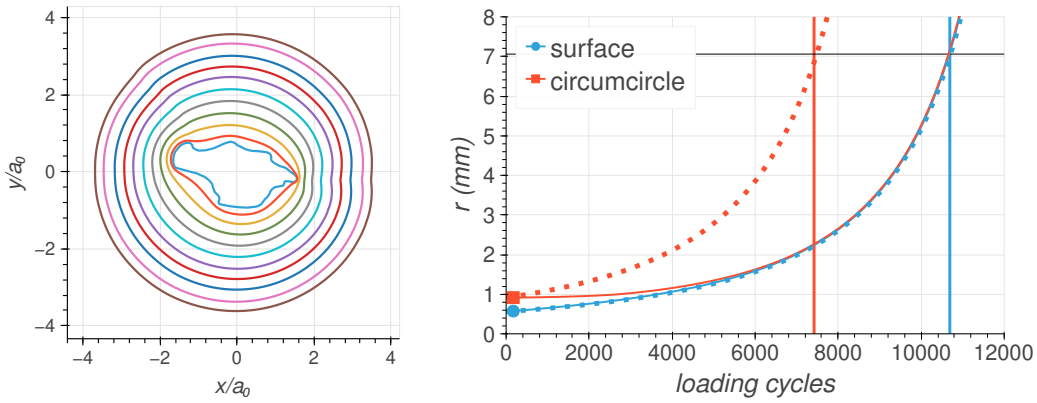

(a) Successive positions of the crack

(b) Evolution of the sizes during propagation

Figure 9: Evolution of the crack obtained by the perturbation approach. The initial shape corresponds to the projection of the defect of Fig. 8 on the orthogonal plane to the load direction.

that the crack surface area should be conserved in any simplification of the crack geometry.

Since the exact shape has a weak influence, it means in particular, that it is more accurate to replace oval shape defects, by circular cracks of same area than to use an external elliptical crack. To illustrate this point further, we also consider another substitution allowing an analytical prediction of lifetime : the substitution by an elliptical crack enclosing the real crack. Some commercial lifetime assessment software such as DARWIN [18] permits the simulation of elliptical cracks by assuming the crack stays elliptical throughout its propagation, and by computing crack advances only at the ends of the minor and major axes of the ellipse. In our case, the starting crack is enclosed by an ellipse having a semi-major axis of 0.98 mm and semi-minor axis of 0.48 mm. We find that Irwin's criterion is reached after 9134 loading cycles.

This value is larger than the one obtained starting from the external circular crack. It was expected since we now know that the crack ultimately becomes circular, the additional cycles correspond to the increase of surface required to transition from the ellipse ($S = 1.5$ mm^2) to the circle ($S = 2.7$ mm^2). Anyway, even if less conservative than the prediction using the circumscribed circle, it still underestimates greatly the real lifetime that would be possible to obtain very easily by taking a circle of same area.

3. Conclusion

Using an iterative perturbative method whose main advantages are to restrict the meshing operations to that of the initial crack front, and to focus on its deformation, we underline the key role of the crack surface area in lifetime predictions. In particular, we show that under the hypotheses of a plane crack uniformly loaded in tensile mode I in an infinite media:

1. The shape evolves quickly toward a circular one, even for complex initial forms.
2. The surface area is an objective way to define an equivalent crack size that leads to irreversible crack advance contrary to other choices.
3. The evolution of the crack surface area due to its propagation in fatigue is weakly dependent on the shape of the crack.
4. Using the fact that cracks of equal area have therefore similar lifetimes in fatigue, it is possible to refine damage tolerant design by using circular cracks with an area equal to that of the original crack. Invoking more complex shapes as ellipses for instance is not useful.

Next steps are to lift certain hypotheses made here to study the effect of complex loading conditions [12], non-uniform remote loading [10], finite size domains. In this effort, it shall be kept in mind that the surface area has to be considered as an objective key parameter to monitor the crack evolution, as demonstrated here in the simplest possible case.

Acknowledgments

The authors acknowledge the financial support of Safran Aircraft Engines to this research work, and in particular Raùl De Moura Pinho for his comments on this work and for providing the tomography image used in Fig. 8. Most data visualizations are made using the *holoviews* python library [19].

Appendix A. Accuracy of the simulation procedure

In section 1.3, we described the method we use to both compute the SIF of the starting cracks we consider in the study and simulate their growth in fatigue.

Here we ensure that this procedure yields precise enough results to consider the obtained simulations as valid. For an elliptic crack loaded remotely by a uniform stress σ of aspect ratio $\alpha = a/b$ where a is the semi-minor axis and b the semi-major axis, the SIF along the front is known analytically (see for example [20]) :

$$K(\theta) = \frac{\sigma\sqrt{a\pi}}{\mathrm{E}(\sqrt{1-\alpha^2})}\left(\frac{\sin^2(\theta)+\alpha^4\cos^2(\theta)}{\sin^2(\theta)+\alpha^2\cos^2(\theta)}\right)^{1/4} \tag{A.1}$$

where θ is the polar position along the crack front relative to the major axis, and E() the elliptic integral of the second kind. We can compare the SIF

obtained by our algorithm to this analytical reference, and as a measure of the numerical error, we compute the maximal relative error as well as the root-mean-square relative error between the computed SIF $K_{num}(s)$ and the analytical SIF $K(s)$ given by equation (A.1) as follows :

$$\text{maximal error} = \frac{1}{K(\theta = 0)} \max_{s \in \mathcal{F}} |K_{num}(s) - K(\theta(s))|$$

$$\text{RMS error} = \frac{1}{K(\theta = 0)} \sqrt{\frac{\int_{\mathcal{F}} |K_{num}(s) - K(\theta(s))|^2 \, \mathrm{d}s}{\int_{\mathcal{F}} \mathrm{d}s}}$$

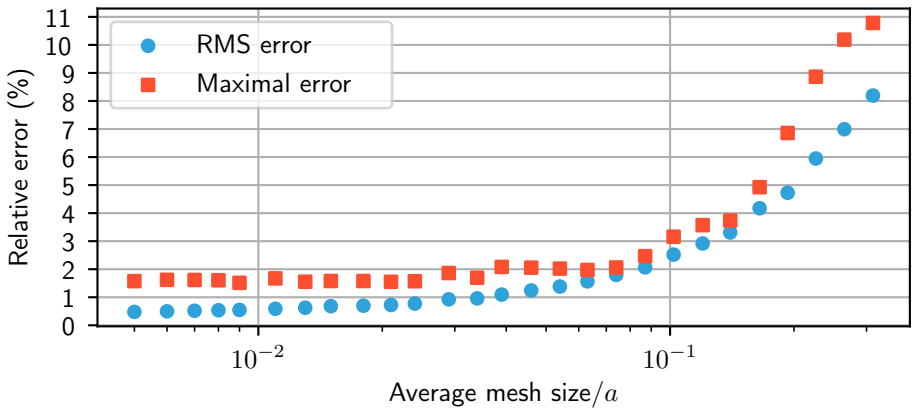

Figure A.10: Relative error of the SIF computed by the iterative perturbation approach in the initialization phase for the case of an elliptical crack with $\alpha = 1/3$.

In figure A.10, these quantities are plotted as a function of the average mesh size for the case of an ellipse with $\alpha = 1/3$. We see that for a sufficiently fine meshing of the crack front, the precision of the computation converges towards a low relative error ($\simeq 1\%$). In our study, we ensured that the meshes are always fine enough to reach this convergence.

To take into account the numerical error that might arise during the second stage of the procedure corresponding to the propagation of the crack, we assessed the numerical error accumulated throughout the whole numerical procedure by recalculating the SIF of the final nearly circular crack by starting from the closest circular crack (see section 1.6). Since this procedure is similar to the one used above for the elliptical crack and even involves fewer iterations since the final shape is nearly circular, the error committed on this final SIF is thus less than 1%. This precise value of the final SIF is compared to the one given by the fatigue propagation simulation (Eq. 11). Since we ensured that this difference is small ($E < 5\%$), we can conclude that the error level throughout the whole simulation is acceptable.

Appendix B. Role of numerical inaccuracies on the variability of $\overline{N}(r/r_0)$ with the crack shape

The dispersion of the curves within the bundles of Fig. 7 has two possible origins : the effect of the crack shape and numerical inaccuracies. In Section 2.5, we announced that this dispersion is at least in part due to the second one. Here we aim to further discuss this affirmation. Only the surface based size will be considered (Fig. 7a).

To quantify the thickness of a bundle, denote $\delta\overline{N}_i(r/r_0) = \frac{\left|\overline{N}-\overline{N}_{circle}\right|}{\overline{N}_{circle}}$ the relative error in predicted lifetime at size r/r_0 for a given crack i. The thickness of the bundle is then naturally defined as :

$$\delta\overline{N}(r/r_0) = \max_{i \in \text{all shapes such as } E<E_{th}} \delta\overline{N_i}(r/r_0) \tag{B.1}$$

This value depends on the Paris exponent n and the tolerance threshold E_{th}

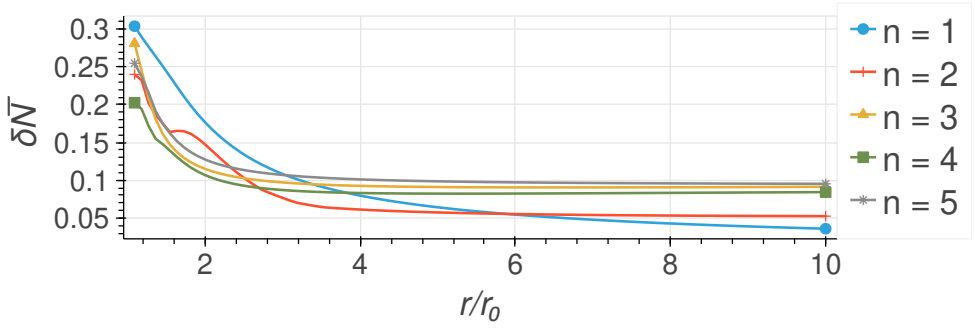

(a) Evolution of the bundle thickness $\delta\overline{N}$ for an error threshold of $E < 0.05$ and different values of n.

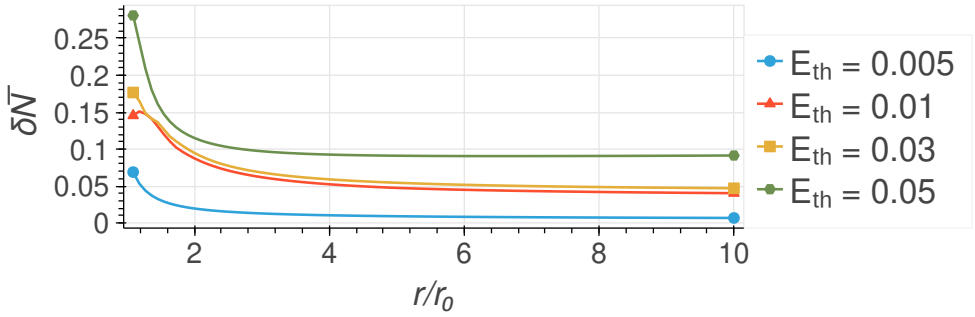

(b) Evolution of the bundle thickness $\delta\overline{N}$ for different error thresholds and $n = 3$.

Figure B.11: Illustration of the stable values reached by $\delta\overline{N}$ for $r/r_0 \to \infty$ for varying values of n and E.

we set on the numerical inaccuracy E for the calculation of K, as defined in Section 1.6 by Eq. 11.

We observe in Fig. B.11, that when r/r_0 increases, $\delta\overline{N}(r/r_0)$ converges towards a constant value $\delta\overline{N}_\infty$ for all values of n and various E_{th}. This is shown in Fig. B.11a for different values of n with a tolerance to numerical error threshold set to $E_{th} = 0.05$, and in Fig. B.11b for $n = 3$ and varying E_{th}. This stabilized value is of interest as it represents the maximal long-term relative error in predicted lifetime made when substituting a crack by a circular crack of equal surface.

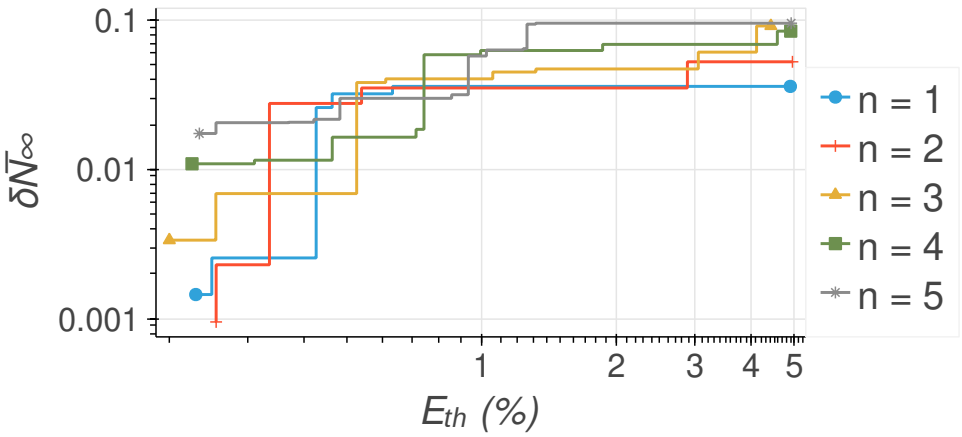

Figure B.12: Decrease of the bundle thickness for decreasing error threshold E, for different values of n. Here, $\delta\overline{N}_\infty$ is taken as $\delta\overline{N}(r/r_0 = 10)$.

For a given value of n, it is clear that $\delta\overline{N}_\infty$ decreases with E_{th} since there are fewer shapes in the set on which the maximum is determined (Eq. B.1). It is confirmed by Fig. B.12 that gives $\delta\overline{N}_\infty$ as a function of E_{th} for different values of n. It remains to be seen whether this decrease can also be attributed at least in part to the numerical errors that the calculation errors on K generate on $\overline{N}$, or equivalently on r/r_0, i.e. the position of the front for a given number of cycles.

To discuss this point, introduce the Bravais-Pearson correlation coefficient r_p between the numerical errors E and $\delta\overline{N}_\infty$. It is defined by:

$$r_p = \frac{\mathrm{cov}(\delta\overline{N}_\infty, E)}{\sigma(\delta\overline{N}_\infty)\sigma(E)} \tag{B.2}$$

where cov is the covariance of two variables and $\sigma(.)$, the standard deviation of a variable $(.)$. $r_p = 0$ signifies absence of correlation, $0 < r_p \leq 1$ a positive correlation (mutual increase of both variables) with $r_p = 1$ corresponding to strict proportionality.

Paris exponent n	1	2	3	4	5
Pearson correlation coefficient r_p	0.20	0.47	0.57	0.58	0.64

Table B.2: Pearson correlation coefficient of E_{th} with $\delta\overline{N}_\infty$ for different values of n

Table B.2 gives the value of r_p for each value of n. The values are larger than 0, which indicates as expected from Fig. B.12, a positive correlation between E and $\delta\overline{N}_\infty$. The correlation coefficient r_p is observed to increase with n. If the numerical error committed in the calculation of K had no consequence on the width of the bundle, there would be no reason to have this positive correlation between n and r_p. Indeed, a numerical error on K has no consequence on the prediction of the shapes in the limiting case where $n = 0$ because the Paris law (Eq. 1) is then independent of K, and has increasingly large consequences when n increases. Hence, this positive correlation tips the balance in favour of the existence of a real causality between numerical errors and thick bundles.

This conclusion allows us to affirm that the influence of the shape of a crack on the fatigue evolution of its surface is weaker than what Fig. 7 suggests. However, we cannot conclude that no influence exists. Since numerical error can never be eliminated completely and the correlation shown here is moderate, only an analytical proof would allow us to concur to an eventual complete absence of influence of the crack shape on the fatigue growth of its surface. In the absence of such a demonstration, or conversely of counter examples, we believe that the numerical method used here, focusing on the crack front alone, is the best to support this conclusion, and that the cor-

relation shown above is the best hint that there is indeed a causal relation between the numerical errors and small variations of crack surface growth from one shape to another.

References

[1] H. Tada, P. C. Paris, G. R. Irwin, The Stress Analysis of Cracks Handbook, Professional Engineering Publishing, 2000.

[2] J. C. Newman Jr, I. S. Raju, Stress-intensity factor equations for cracks in three-dimensional finite bodies, NASA Technical Memorandum 83200 (1981).

[3] V. Lazarus, Perturbation approaches of a planar crack in linear elastic fracture mechanics: a review, Journal of the Mechanics and Physics of Solids 59 (2011) 121–144. doi:10.1016/j.jmps.2010.12.006.

[4] H. F. Bueckner, Weight functions and fundamental fields for the penny-shaped and the half-plane crack in three-space, International Journal of Solids and Structures 23 (1987) 57–93.

[5] J. R. Rice, First-order variation in elastic fields due to variation in location of a planar crack front, ASME Journal of Applied Mechanics 52 (1985) 571–579.

[6] J. R. Rice, Weight function theory for three-dimensional elastic crack analysis, in: R. P. Wei, R. P. Gangloff (Eds.), Fracture Mechanics : Perspectives and Directions (Twentieth Symposium), American Society

for Testing and Materials STP 1020, Philadelphia, USA, 1989, pp. 29–57.

[7] A. F. Bower, M. Ortiz, Solution of three-dimensional crack problems by a finite perturbation method, Journal of the Mechanics and Physics of Solids 38 (1990) 443–480.

[8] A. F. Bower, M. Ortiz, A three-dimensional analysis of crack trapping and bridging by tough particles, Journal of the Mechanics and Physics of Solids 39 (1991) 815–858.

[9] A. F. Bower, M. Ortiz, The influence of grain size on the toughness of monolithic ceramics, Transactions of the ASME. Journal of engineering materials and technology. 115 (1993) 228–236.

[10] A. F. Bower, M. Ortiz, An analysis of crack trapping by residual stresses in brittle solids, Transactions of the ASME. Journal of Applied Mechanics 60 (1993) 175–82.

[11] V. Lazarus, Brittle fracture and fatigue propagation paths of 3D plane cracks under uniform remote tensile loading, International Journal of Fracture 122 (2003) 23–46. doi:10.1023/B:FRAC.0000005373.73286.5d.

[12] E. Favier, V. Lazarus, J.-B. Leblond, Coplanar propagation paths of 3D cracks in infinite bodies loaded in shear, International Journal of Solids and Structures 43 (2006) 2091–2109. doi:10.1016/j.ijsolstr.2005.06.041.

[13] M. Vasoya, V. Lazarus, L. Ponson, Bridging micro to macroscale fracture properties in highly heterogeneous brittle solids: weak pinning versus

fingering, Journal of the Mechanics and Physics of Solids 95 (2016) 755–773. doi:http://dx.doi.org/10.1016/j.jmps.2016.04.022.

[14] L. Legrand, V. Lazarus, Front shape and loading evolution during cracks coalescence using an incremental perturbation method, Engineering Fracture Mechanics 133 (2015) 40–51. doi:10.1016/j.engfracmech.2014.10.026.

[15] H. Gao, J. R. Rice, Somewhat circular tensile cracks, International Journal of Fracture 33 (1987) 155–174.

[16] N. Fleck, K. Kang, M. Ashby, Overview no. 112: The cyclic properties of engineering materials, Acta Metallurgica et Materialia 42 (1994) 365–381. doi:10.1016/0956-7151(94)90493-6.

[17] B. Gärtner, Fast and robust smallest enclosing balls, in: European symposium on algorithms, Springer, 1999, pp. 325–338.

[18] Southwest Research Institute, Darwin, 2017. URL: `https://www.swri.org/darwin`.

[19] P. Rudiger, J.-L. Stevens, J. A. Bednar, B. Nijholt, J. Mease, Andrew, C. B, A. Randelhoff, V. Tenner, maxalbert, M. Kaiser, ea42gh, J. Samuels, stonebig, K. Pevey, F. LB, A. Tolmie, D. Stephan, Hoxbro, J. Bois, S. Lowe, J. Bampton, henriqueribeiro, ruoyu0088, I. Lustig, A. Klein, B. V. de Ven, J. Signell, L. Talirz, L. Barth, holoviz/holoviews: Version 1.14.2, 2021. URL: `https://doi.org/10.5281/zenodo.4581995`. doi:10.5281/zenodo.4581995.

[20] G. R. Irwin, Crack-extension force for a part-through crack in a plate, ASME Journal of Applied Mechanics 29 (1962) 651–661.